




# Durable shape sensor based on FBG array inscribed in polyimide-coated multicore optical fiber

KIRILL BRONNIKOV,<sup>1,2,\*</sup>  ALEXEY WOLF,<sup>1,2</sup> SERGEY YAKUSHIN,<sup>2,3</sup> ALEXANDR DOSTOVALOV,<sup>1,2</sup> OLGA EGOROVA,<sup>4</sup> SERGEY ZHURAVLEV,<sup>5</sup> SERGEY SEMJONOV,<sup>5</sup> STEFAN WABNITZ,<sup>2,6</sup>  AND SERGEY BABIN<sup>1,2</sup>

<sup>1</sup>*Institute of Automation and Electrometry of the SB RAS, 1 Acad. Koptuyug Ave., Novosibirsk, 630090, Russia*

<sup>2</sup>*Novosibirsk State University, 2 Pirogova St., Novosibirsk, 630090, Russia*

<sup>3</sup>*SibSensor LLC, 20 Inzhenernaya Str., Novosibirsk, 630090, Russia*

<sup>4</sup>*Prokhorov General Physics Institute of the Russian Academy of Sciences, Moscow, Russia*

<sup>5</sup>*Fiber Optics Research Center of the RAS, Moscow, Russia*

<sup>6</sup>*Dipartimento di Ingegneria dell'Informazione, Elettronica e Telecomunicazioni, Sapienza Università di Roma, Roma, Italy*

\*[bronnikovkirill@gmail.com](mailto:bronnikovkirill@gmail.com)

**Abstract:** The paper presents a novel three-dimensional quasi-continuous shape sensor based on an FBG array inscribed by femtosecond laser pulses into a 7-core optical fiber with a polyimide protective coating. The measured bending sensitivity of individual FBGs ranges from 0.046 nm/m<sup>-1</sup> to 0.049 nm/m<sup>-1</sup>. It is shown that the sensor allows for reconstructing 2- and 3-dimensional shapes with high accuracy. Due to the high value of the core aperture and individual calibration of each FBG we were able to measure the smallest reported bending radii down to 2.6 mm with a record accuracy of ~1%. Moreover, we investigate the magnitude of the errors of curves reconstruction and errors associated with measurement of curvature radii in the range from 2.6 to 500 mm. The main factors affecting the accuracy of measurements are also discussed. The temperature resistance of both the inscribed FBG structures and of the protective coating, along with the high mechanical strength of the polyimide, makes it possible to use the sensor in harsh environments or in medical and composite material applications.

© 2019 Optical Society of America under the terms of the [OSA Open Access Publishing Agreement](#)

## 1. Introduction

Currently, multi-core optical fibers (MCFs), with both straight and twisted cores, are being actively studied for creating compact distributed bending sensors or shape sensors [1,2]. Such sensors are used in micro-robotics, in particular in devices for minimally invasive surgery, as well as in monitoring the structural state of objects subject to bending and torsion [3,4]. When the cores do not have a cross talk, two different approaches to interrogating MCF-based sensors are predominantly used. The first approach involves the method of high-resolution backscatter reflectometry; the second is based on the analysis of the resonance spectra of 3-dimensional arrays of fiber Bragg gratings (FBGs), inscribed in different cores along the MCF. The advantage of the reflectometry method, which can provide up to ~10 microns resolution when measuring the longitudinal strain of the MCF [5], is the continuity of the measurement, as well as the relatively longer length of the interrogated section of MCF. However, the high cost of this type of device, and the low interrogation rate limit the use of the reflectometry method in some practical applications. At the same time, sensors based on FBG arrays, which are interrogated by using a spectral interrogator, allow for quasi-continuous shape reconstruction for lengths of 0.01–1 m.

The advantages of this method include: the significantly lower cost of the interrogating device, high interrogation rates (up to 10 kHz), and simplicity of the shape reconstruction algorithms, which makes real-time reconstruction possible [6].

In a number of applications, an important factor in the operation of shape sensors based on MCF is their mechanical and temperature “endurance”. This requirement applies both to the protective coating material of the fiber, as well as to the modified part of the MCF, in which the FBG array is inscribed. In particular, when the MCF is embedded in a composite material, a high degree of adhesion of the protective coating with the glass cladding of the optical fiber and with the external material is required [7,8]. During the curing of composite materials, such as carbon fiber prepreps, the temperature can reach 180 °C for epoxy/carbon fiber composites [9], and 350 °C for polyimide/carbon fiber composites [10]. In addition, the temperature resistance of sensors involving FBGs is an important factor in the sterilization of a medical device by heat treatment in an autoclave. At these high temperatures, degradation and destruction of such protective coating as acrylate take place [11]. At the same time, FBGs fabricated by UV radiation may experience a temperature degradation of the reflection coefficient [12]. One of the most promising and durable protective polymer coatings of optical fibers is polyimide, which can be exposed to a prolonged high temperature impact up to 300 °C, and short-term up to 350–400 °C. The femtosecond micromachining technology inside the volume of transparent dielectric materials [13] allows for FBG inscription through a polyimide coating without its damage [14], which preserves the mechanical properties of the fiber surface. Moreover, FBGs created by using the femtosecond technology demonstrate a significant temperature and mechanical durability [15], which makes this approach promising for creating durable shape sensors for various applications.

In this article, we report on the results of the fabrication and testing of 3-dimensional FBG arrays in a 7-core custom-made optical fiber with a polyimide coating. By using the direct femtosecond inscription method, an array was created with a total length of 72 mm, consisting of 24 FBGs inscribed in 6 cross-sections (nodes) of the MCF. For this array, 2- and 3-dimensional shapes are reconstructed. The measurements were carried out in wide range of radius of curvature from 2.6 mm to 500 mm. The factors limiting the curvature measurements range are presented.

## 2. 3D FBG array shape reconstruction

### 2.1. Curvature vector calculation

The problem of reconstructing the shape of an MCF involves calculating the curvatures and curvature directions for each point along the fiber. By knowing these parameters, it is possible to construct a spatial curve in a parametric form, for example, by using Frenet-Serret differential equations [16]. When using arrays consisting of separate FBGs, the curvature vectors are only determined at certain discrete points, and the spatial resolution of the sensor is given by the inverse distance between neighboring gratings.

Consider a cross-section of an MCF with FBGs inscribed in the side cores (Fig. 1). For a definite measurement of the curvature vector in an MCF, typically three cores are used, which are located at the vertices of an equilateral triangle: such a configuration was chosen in this paper. To calculate the curvature under bending deformation, we used the approach proposed in [16]. It consists in considering the partial curvature vectors for each  $i$ -th side core:

$$\kappa_i = -\frac{1}{r_c}(\varepsilon_i \cos \alpha_i \mathbf{n}_x + \varepsilon_i \sin \alpha_i \mathbf{n}_y), \quad (1)$$

where  $r_c$  is the distance between the centers of the fiber and core  $i$ ,  $\varepsilon_i$  is the strain associated with a length change,  $\alpha_i$  is the angle between the direction to the core and the local  $x$  axis,  $\mathbf{n}_x$  and  $\mathbf{n}_y$  are unit vectors for the  $x$  and  $y$  axes, respectively. The  $\kappa_i$  vector points in the direction of the  $i$ -th core from the center of the MCF (or in the opposite direction, depending on the sign of  $\varepsilon_i$ ). The

relationship between the FBG deformation  $\varepsilon_i$  and a change in its resonant wavelength  $\Delta\lambda_i$  can be derived from the following differential equation [17]:

$$\frac{d\lambda}{\lambda} = C\varepsilon + \Omega dT, \quad (2)$$

where  $\lambda$  is the wavelength,  $\varepsilon$  is the strain,  $C = (1 - p)$ , where  $p$  is the strain-optic coefficient,  $\Omega$  is the temperature sensitivity, and  $T$  is the temperature. Here we take an approximate dependence with the following replacements:  $d\lambda \rightarrow \Delta\lambda$ ,  $\lambda \rightarrow \lambda^B$ , and we exclude the temperature dependence, which will be taken into account by using data from FBGs in the central core (this will be explained in more detail in Section 4). Thus, for the  $i$ -th core, one obtains:

$$\varepsilon_i = \frac{1}{C_i} \frac{\Delta\lambda_i}{\lambda_i^B}, \quad (3)$$

where  $C_i$  is the strain coefficient, which will be determined during the calibration process, and  $\lambda_i^B$  is the Bragg wavelength of the FBG in the straight unstressed state.

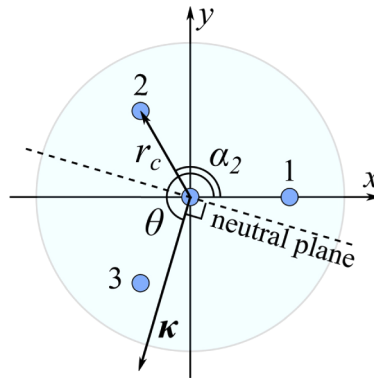


**Fig. 1.** Multi-core fiber cross-section sketch, and relevant parameters for curvature calculation.

To find the total curvature vector in a given node with  $N$  cores, the averaged sum of the  $\kappa_i$  vectors is calculated:

$$\kappa = -\frac{2}{Nr_c} \left( \sum_{i=1}^N \varepsilon_i \cos \alpha_i \mathbf{n}_x + \sum_{i=1}^N \varepsilon_i \sin \alpha_i \mathbf{n}_y \right). \quad (4)$$

Then the direction of curvature is  $\theta = \text{angle}(\kappa)$ . Calculating  $\kappa$  in each FBG node gives a discrete set of vectors  $\{\kappa_{j=1 \dots n}\}$ , where  $j$  is the number of the node, and  $n$  is the total number of nodes. This set is interpolated by a cubic spline to obtain a vector function  $\kappa(s)$ , where  $s$  is the length along the fiber.

## 2.2. Frenet-Serret framework

A spatial curve can be defined by the Frenet-Serret equations [18]:

$$\begin{cases} \mathbf{r}'(s) = \mathbf{T}(s) \\ \mathbf{T}'(s) = \kappa(s)\mathbf{N}(s) \\ \mathbf{N}'(s) = \tau(s)\mathbf{B}(s) - \kappa(s)\mathbf{T}(s) \\ \mathbf{B}'(s) = -\tau(s)\mathbf{N}(s) \end{cases}. \quad (5)$$

Here,  $s$  is a length parameter,  $\mathbf{r}(s)$  is the position vector defining the parametric curve in space,  $\mathbf{T}(s)$  is the unit vector tangent to the curve at point  $s$ ,  $\mathbf{N}(s)$  is the normal unit vector directed towards the center of curvature,  $\mathbf{B}(s)$  is the binormal unit vector perpendicular to the vectors  $\mathbf{T}(s)$  and  $\mathbf{N}(s)$ :  $\mathbf{B}(s) = \mathbf{T}(s) \times \mathbf{N}(s)$ , where  $\times$  denotes a vector product. The three vectors  $\mathbf{T}(s)$ ,  $\mathbf{N}(s)$  and  $\mathbf{B}(s)$  form an orthogonal basis in  $\mathbb{R}^3$ . The scalar functions  $\kappa(s)$  and  $\tau(s)$  are called the curvature and the torsion of a parametric curve, respectively. If these functions are known in explicit form, then by solving the system of Eq. (5), one can construct a curve  $\mathbf{r}(s) = \int_0^L \mathbf{T}(s)ds + \mathbf{r}_0$ , where  $L$  is the length of the curve, and  $\mathbf{r}_0$  is the initial position at  $s = 0$ .

In our case, the curvature and torsion are obtained from the interpolation vector function  $\kappa(s)$  mentioned earlier:  $\kappa(s) = |\kappa(s)|$  and  $\theta(s) = \text{angle}(\kappa(s))$ . When substituting this to Eq. (5),  $\kappa(s)$  is assumed unchanged, and  $\tau(s) = \theta'(s)$ . To solve Eq. (5), it is also necessary to set the initial values of all four vector functions  $\mathbf{r}(s)$ ,  $\mathbf{T}(s)$ ,  $\mathbf{N}(s)$  and  $\mathbf{B}(s)$  at  $s_0 = 0$ . The starting point of the curve  $\mathbf{r}_0$  can be chosen arbitrarily, and let to coincide with the origin:  $\mathbf{r}_0 = (0, 0, 0)$ . The tangential vector  $\mathbf{T}_0$  determines the direction of increasing the length of the curve at the starting point and it can also be selected for reasons of convenience, so we direct it along one of the coordinate axes:  $\mathbf{T}_0 = (1, 0, 0)$ . The normal vector  $\mathbf{N}_0$  should be perpendicular to  $\mathbf{T}_0$ , and is determined by the direction to the center of curvature at point  $s_0$ , i.e., by the value of the interpolated function  $\theta_0 = \theta(s_0)$ :  $\mathbf{N}_0 = (0, \cos \theta_0, \sin \theta_0)$ . The initial binormal vector  $\mathbf{B}_0$  is defined according to:  $\mathbf{B}_0 = \mathbf{T}_0 \times \mathbf{N}_0$ .

This method assumes that the angular orientation of the cores relative to the  $x, y$  coordinate axes, which is defined at the beginning of the fiber section with inscribed FBG array, remains constant along the entire fiber length. If this condition is violated, i.e., there is an external twist of the fiber around its central axis, then errors in determining the direction of bending appear and, subsequently, the total error in the fiber shape reconstruction increases. To compensate for this drawback, the use of multi-core spun fibers seems to be a promising approach, where the natural twist of the cores enables measuring the magnitude and direction of the external twist [19].

### 3. FBGs inscription in polyimide-coated MCF

Previously, a selective inscription of FBGs in MCFs was realized using the method utilizing UV radiation with a phase mask [20] and point-by-point inscription by femtosecond laser pulses [21]. In this work, FBG inscription is carried out by using the modified plane-by-plane method [22] with infrared femtosecond pulses produced by Light Conversion Pharos 6W laser (wavelength  $\lambda = 1030$  nm, pulse duration  $t_p = 232$  fs, repetition rate  $f = 1$  kHz). We use a Mitutoyo 50X Plan Apo NIR HR objective ( $NA = 0.65$ ) and an additional cylindrical lens with a focal distance  $f_c = -1000$  mm, mounted before the objective, in order to focus fs pulses into a given volume of MCF. A special glass ferrule with polished side faces makes it possible to fix the position of the MCF with respect to the focal point, as described in detail in our previous works [14,23]. The longitudinal periodic modulation of the refractive index is achieved by moving the fiber with a predefined constant velocity  $v_{tr} \approx 1$  mm/s (2<sup>nd</sup> order of Bragg resonance), by using an Aerotech ABL1000 high-precision air-bearing linear stage. Thus, the FBG period is determined by  $\Lambda = v_{tr}/f$ , and the resonant wavelength by  $\lambda^B = 2n_{eff}v_{tr}/(mf)$ , where  $m = 2$  is the order in which resonant reflection of the optical signal on the FBG structure is realized. When writing FBGs, the tail of the MCF is fixed on the linear stage with the help of a clamp, with an angular degree of freedom allowing to turn the fiber around its axis.

A sample of an FBG array was inscribed in a 7-core optical fiber manufactured at the Fiber Optics Research Center of the Russian Academy of Sciences (FORC RAS, Moscow, Russia), whose parameters are summarized in Table 1. The separation of optical signals from individual MCF cores is carried out by using a specialized fan-out device, which provides a back reflection coefficient of less than  $-40$  dB at the junction with the MCF, and the level of insertion optical

loss of less than 1 dB. The fan-out was manufactured and connected to the MCF in the same way as described in [24].

**Table 1. Parameters of the used polyimide-coated 7-core optical fiber**

Parameter	Value
Cores arrangement	Hexagonal + central core
Protective coating material	Polyimide
Cladding diameter	125 $\mu\text{m}$
Coating diameter	154 $\mu\text{m}$
Cores separation distance	40.5 $\mu\text{m}$
Cut-off wavelength	1450–1490 nm
Attenuation	1 dB/km @ 1550 nm
Numerical aperture	0.21
Mode field diameter	5.7 $\mu\text{m}$ @ 1550 nm

The fiber is coated with a  $\sim 10 \mu\text{m}$  polyimide protective layer, thus giving the outer fiber diameter of 154 microns. Polyimide coating makes it possible to use the fiber at high temperatures (up to 300  $^{\circ}\text{C}$ ), and with direct mechanical impacts, since it has a higher hardness as compared to standard acrylate, as well as high adhesion to the glass surface of the fiber cladding. This advantage allows using this fiber to create high-temperature optical sensors for structural monitoring in a harsh environment, such as nuclear facilities, where the sensor might be a subject to prolonged high-temperature exposure (up to 200–250  $^{\circ}\text{C}$ ) [25]. In addition, the relatively small diameter of the fiber facilitates the incorporation of the fiber-optic sensor into various designs, for example, in the production of “smart” composite materials [9].

A sample of an FBG array consisting of 6 nodes along the fiber, with an interval between the centers of the nodes  $\Delta L = 14 \text{ mm}$ , was inscribed in the above described fiber. In each node, FBG inscription was carried out in the central core, and in three side cores located at the corners of an equilateral triangle. Each of the FBGs in the array had a uniform refractive index profile and a fixed length of  $L_{\text{FBG}} = 2 \text{ mm}$ ; the total length of the FBG array was  $L = 72 \text{ mm}$ . A schematic representation of the created sample, as well as the FBG numbering in the array, is shown in Fig. 2. Four FBGs in the same node have equal physical periods  $\Lambda$ ; for the spectral separation of FBG resonances along the same core in different nodes, the FBG physical periods varied sequentially from  $\Lambda_1 = 1.0353 \mu\text{m}$  to  $\Lambda_6 = 1.0939 \mu\text{m}$ . The change in the period by  $\Delta\Lambda \approx 11.7$

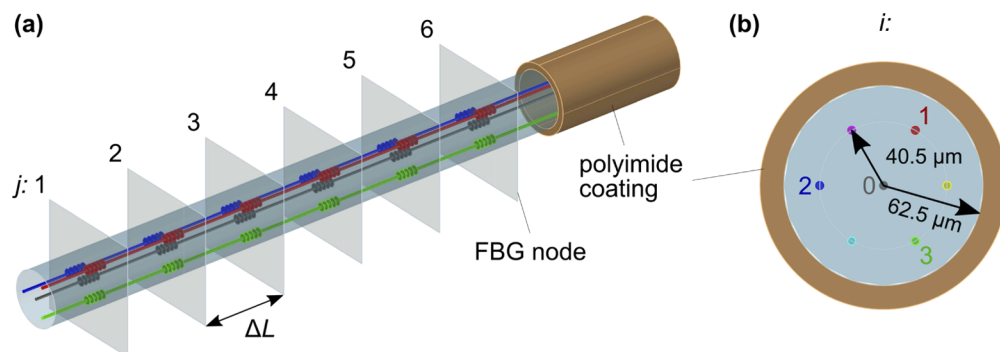


**Fig. 2.** Schematic representation of the FBG array inscribed in 7-core optical fiber through polyimide protective coating: (a) 3D representation, and (b) transverse cross section of the used MCF.

nm between adjacent nodes allowed for the spectral separation of their resonances by  $\Delta\lambda \approx 16.7$  nm. The sequential change of cores during the writing process was carried out by the transverse displacement of the MCF relative to the focus of writing objective. An example of the reflection/transmission spectra measured for one of the cores of the array by using Yokogawa AQ6370D optical spectrum analyzer is presented in Fig. 3. In our case, the relatively strong resonances of the “ghost” modes [26], which are observed in transmission spectra close to  $\lambda^B$  on the short wavelength side, can be attributed to the presence of a weak tilt of the grating planes, or to the specifics of the inscription method resulting in the inscription of grating planes beyond the core boundaries and, in this way, facilitating the propagation of ghost modes.

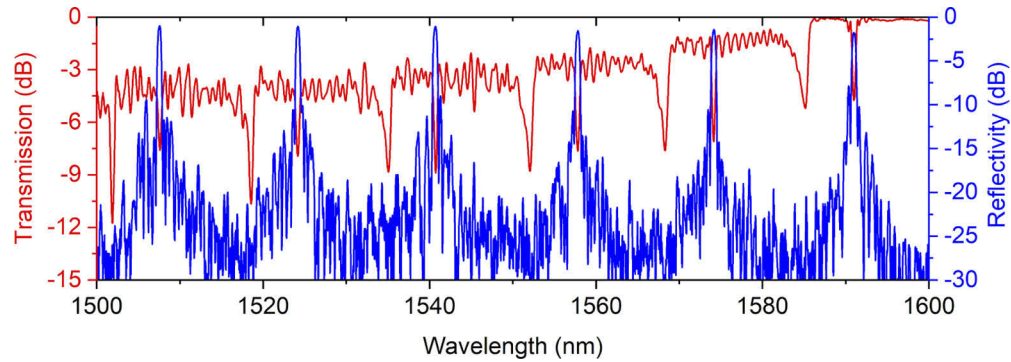


**Fig. 3.** Reflection/transmission spectra of the FBG array measured for one of the cores of the 7-core optical fiber.

To interrogate the fabricated shape sensor, we used a HBM FS22-SI 8-channel interrogation unit providing a single measurement of all cores per second (Fig. 4). The unit has wavelength resolution/repeatability of  $<0.5$  pm, wavelength stability/reproducibility of 1 pm, and dynamic range of  $>50$  dB. Processing of the measured spectra, detection and tracking of the FBG reflection peaks, was maintained with the BraggMONITOR SI application.

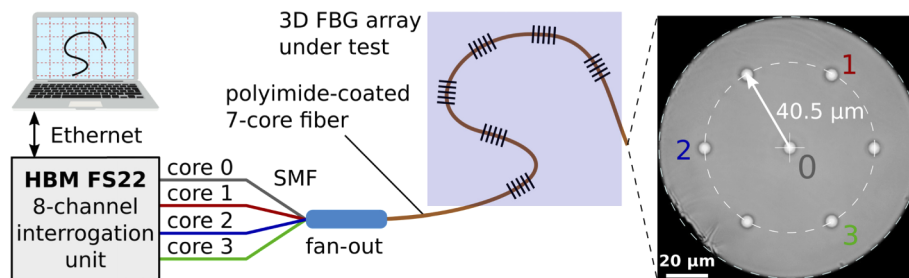


**Fig. 4.** Interrogation scheme of shape sensor based on a FBG array in a 7-core optical fiber.

#### 4. FBG array calibration

Errors in the arrangement of the cores and of the FBGs in the cross-section of the MCF, along with the presence of fluctuations in the refractive index of the cores, introduce a variation in the bending sensitivity coefficients of individual FBGs. In order to take into account the above factors, and to achieve maximum accuracy when reconstructing the shape of the sensor, we took a series of calibration measurements.



For calibration, we used a set of arc grooves machined on an acrylic glass plate. The arcs had different constant radii of curvature, ranging from 10 to 100 mm. Teflon tubes arranged in the arcs limited the movement of the fiber. At the entrance of a groove, the MCF was fixed with a graduated rotating clamp, so that the calibrated FBG node was located inside the groove, while the end of the fiber remained free. After that, the fiber was rotated around its axis in 5 degrees increments. On each groove, a full turn of the MCF was performed, during which the reflection spectra of the FBG array were measured. Maximum deformation of a separate FBG in the side core (positive and negative) is achieved when an FBG is located in the plane of the bend. Conversely, minimum deformation will occur when the FBG is placed on a neutral surface passing through the central axis of the optical fiber, perpendicularly to the plane of the bend.

FBGs located in the central core practically do not experience the action of bending deformations, but are affected by stretching and temperature changes, which are common to all gratings in a given node. Thus, FBGs in the central core can be used to take into account these effects on remaining FBGs. To exclude the effects, in each measurement the wavelength detuning values of the central core FBGs reflection peaks were subtracted from the side cores FBGs.

Since, even with a small step in the rotation angle, the position of the side core when the maximum deformation occurs can be missed, for a more accurate estimate of the FBG peak wavelength shift at a given curvature an approximation of the data was used. The distance from the FBG to the neutral plane is proportional to the cosine of the angle between the bending direction and the straight line passing through the FBG and the central axis of the fiber. Therefore, an offset sinusoid is taken for approximation (Fig. 5(a)).

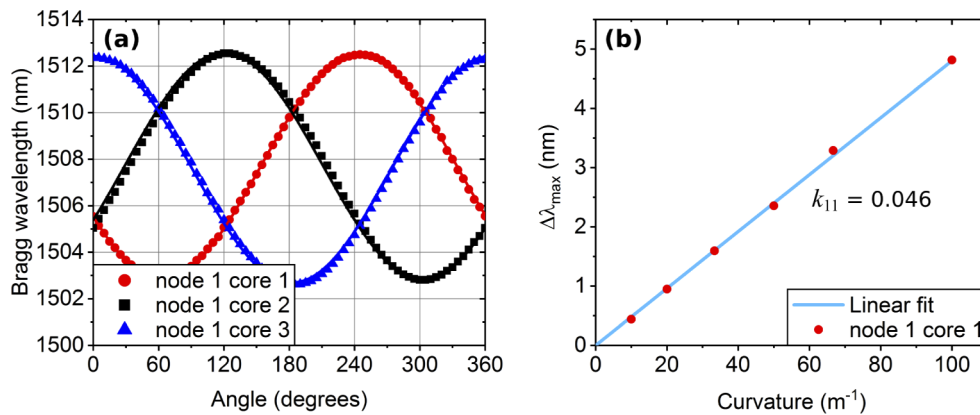


**Fig. 5.** (a) Dependence of the FBG wavelength on the angle of rotation of the MCF measured for node 1 with a radius of curvature of 10 mm. (b) Maximum FBG wavelength shift measured for the sinusoidal fit curve of the side core 1 in the node 1 versus curvature.

The obtained amplitude of a separate sinusoid will characterize the maximum wavelength shift of the FBG reflection peak. By conducting experiments at different values of the radius of curvature, it is possible to obtain the dependence of the change in the resonant wavelength  $\Delta\lambda_{\max}$  on curvature for each of the FBGs in the array. Next, these dependences were approximated by a linear function with a slope  $k$  [ $\text{nm}/\text{m}^{-1}$ ]:  $\Delta\lambda_{\max} = k/R$ , where  $R$  is the radius of curvature. Since  $\varepsilon = r_c/R$  in the position of maximum deformation of FBG, by solving this equation together with Eq. (3), we obtain the expression for the FBG calibration coefficient in the  $i$ -th core in a given node:

$$C_i = \frac{k_i}{r_c \lambda_i^B}. \quad (6)$$

For example, results obtained for the FBGs in node 1 are shown in Fig. 5. In general, for all FBGs in the array, the linear sensitivity coefficient  $k$  took values from  $0.046 \text{ nm/m}^{-1}$  to  $0.049 \text{ nm/m}^{-1}$ .

## 5. Shape measurements and temperature testing

We carried out experiments on reconstructing the shape of an MCF in the case of bending in a plane. First, the reflection spectra were measured for a straight non-stressed fiber, and the corresponding positions of the FBG reflection peaks  $\lambda_{ij}^B$  (where  $i = 0, \dots, 3$  is the core number,  $j = 1, \dots, 6$  is the node number) were determined by using the interrogation scheme described earlier (Fig. 4). After that, in two experiments, a part of the fiber with inscribed FBGs was taped to the table in a loop-like and s-shaped form, and the shifts of FBG resonance wavelengths  $\Delta\lambda_{ij}$  were measured with subtracting the central core shifts from the side ones, in order to compensate for temperature effects and longitudinal strain. From the values  $\Delta\lambda_{ij}$ , the deformations  $\varepsilon_{ij}$  were calculated from Eq. (3), using the coefficients  $C_{ij}$  obtained from the calibration. The fiber shape reconstruction was performed according to the method previously described in Section 2.

As mentioned earlier, our method does not take into account the presence of fiber twist. Therefore, in order to reduce the error due to possible torsions, the ends of the sensor, while in the straight form, were sealed with adhesive tape. In this way, when the fiber is bent, maintaining the mutual orientation of the tape pieces made it possible to maintain the orientation of the cores along the sensor, at least to some extent. The recovered curves superimposed on the respective photographs of the two shapes are shown in Fig. 6.

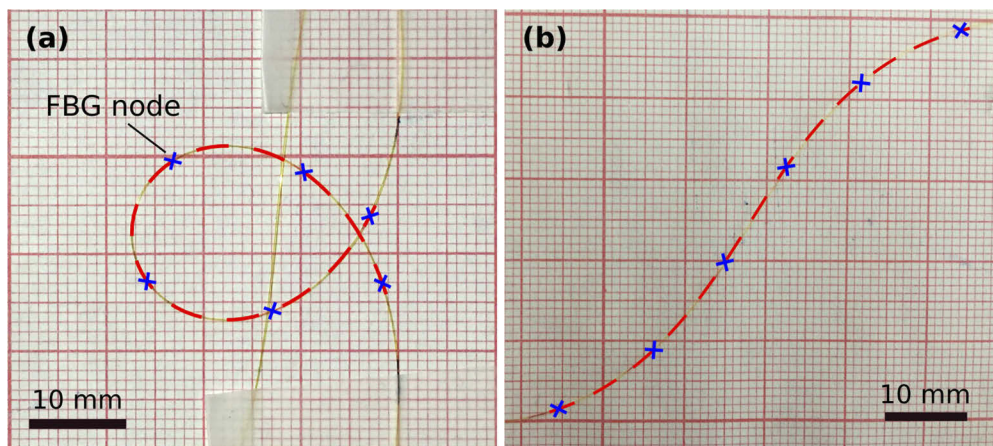


**Fig. 6.** Photos of the MCF with an inscribed FBG array of length  $L = 72 \text{ mm}$ , and calculated curves (red dashed line): (a) a loop-like curve, (b) an s-shaped curve. Blue crosses indicate FBG nodes. In Fig. 6(a), the fiber crossing the loop was used to align the sensor with the plane of the table.

Images reveal that the maximum estimated position error in the picture plane of the planar shape reconstruction did not exceed  $0.2 \text{ mm}$ . To estimate the error in the transverse direction the deviation of the curves from the picture plane was measured and amounted to  $\sim 0.25 \text{ mm}$  for a loop-shaped curve, and  $\sim 0.2 \text{ mm}$  for an s-shaped curve.

Next, experiments on reconstructing the 3D shape of the MCF were carried out. The fiber section with the inscribed FBG array was sequentially wound in the form of a spiral on three cylindrical surfaces with diameters  $D_{\text{spiral}} = 25, 29.5, 38.1$  and  $66 \text{ mm}$ , and with a pitch  $h_{\text{spiral}} = 21, 49, 10$  and  $49 \text{ mm}$ , respectively, with 6 measurements for each curve. The method of fiber shape reconstruction was similar to that used for planar curves. The obtained curves along with the ground truth spirals are presented in Fig. 7. Figure 8 presents the averaged absolute error of



the shape reconstruction  $\delta_{\text{abs}}$  (Fig. 8(a)) and error per unit length  $\delta_{\text{rel}}$  (relative error) (Fig. 8(b)), calculated according to:

$$\delta_{\text{abs}}(s) = \|\mathbf{r}_{\text{meas}}(s) - \mathbf{r}_{\text{ref}}(s)\| \text{ and } \delta_{\text{rel}}(s) = \delta_{\text{abs}}(s)/s, \quad (7)$$

where  $\mathbf{r}_{\text{meas}}(s)$  is the measured position vector defining the parametric curve in space,  $\mathbf{r}_{\text{ref}}(s)$  is the position vector for the ground truth curve,  $s$  is the coordinate along the curve. In Table 2 we provide the mean maximum values of the absolute and relative error for each spiral curve that were obtained by averaging 6 measurements for each curve.

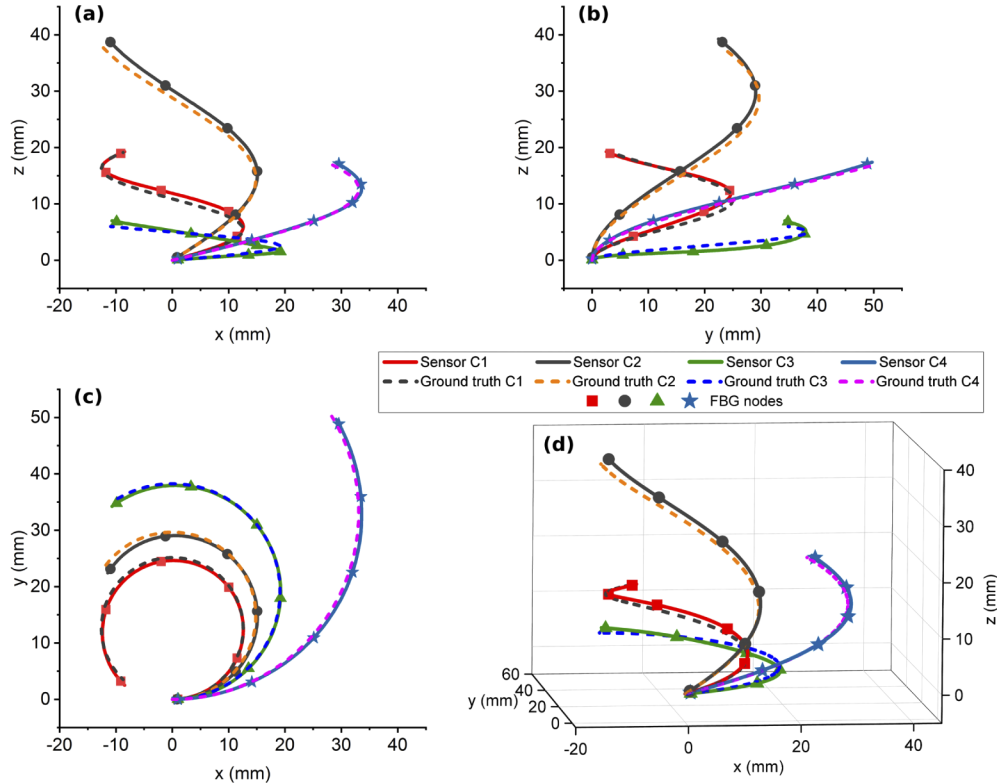


**Fig. 7.** Reconstructed 3D curves and ground truth curves: (a) projection onto  $xz$  plane, (b)  $yz$  plane, (c)  $xy$  plane; (d) 3D view. C1:  $D_{\text{spiral}} = 25$  mm,  $h_{\text{spiral}} = 21$  mm; C2:  $D_{\text{spiral}} = 29.5$  mm,  $h_{\text{spiral}} = 49$  mm; C3:  $D_{\text{spiral}} = 38.1$  mm,  $h_{\text{spiral}} = 10$  mm; C4:  $D_{\text{spiral}} = 66$  mm,  $h_{\text{spiral}} = 49$  mm.

**Table 2. Geometric parameters of the spirals and errors of shape recovery**

Configuration	$D_{\text{spiral}}$ , mm	$h_{\text{spiral}}$ , mm	Max. mean abs. error, mm	Max. mean rel. error, %
C1	25	21	$1.27 \pm 0.89$	$2.04 \pm 1.24$
C2	29.5	49	$1.57 \pm 0.86$	$2.18 \pm 1.45$
C3	38.1	10	$1.08 \pm 0.5$	$1.96 \pm 1.28$
C4	66	49	$0.85 \pm 0.45$	$1.89 \pm 0.86$

We believe that the main sources of errors originate from the presence of an external twist of the fiber sensor around its longitudinal axis as well as the inherent birefringence of FBGs. The

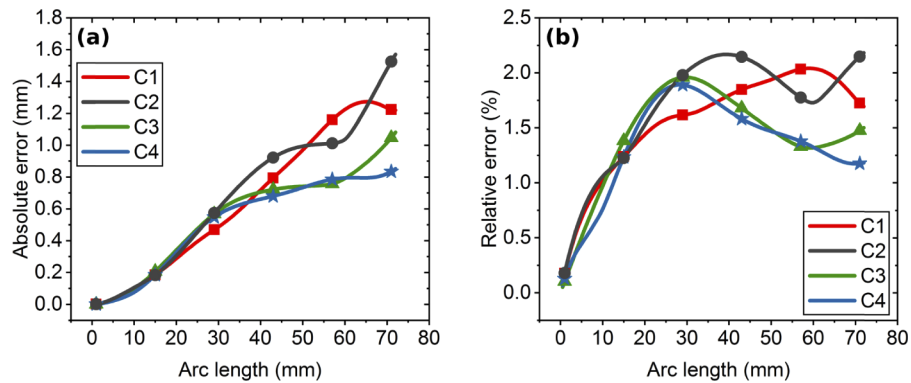


**Fig. 8.** (a) absolute reconstruction error, (b) error per unit length versus arc length.

former leads to errors in the calculation of the bending direction and, consequently, a deviation of the reconstructed curve from the reference one. The influence of the latter is discussed below.

Fiber breakage probability when bending with small radii of curvature can be increased due to defects in the glass cladding of an MCF. In the case of non-UV-transparent coating, FBG inscription using UV light requires recoating procedure, which may cause the appearing of defects. Direct plane-by-plane femtosecond inscription through the protective coating does not require coating removal erasing this disadvantage. Furthermore, the increased mechanical strength of the polyimide, as compared to acrylic coating, makes a fiber more robust to external impacts. Mentioned factors together with the high  $NA$  value of the used MCF suggest the use of the proposed sensor in measurements of extremely small curvature radii. To test the accuracy of the sensor configuration, a sample of an FBG array consisting of a single node with resonant FBG wavelengths located near 1550 nm was fabricated and calibrated. We carried out measurements of large curvatures, and calculated the bending radius dependence of the relative error. The fiber was wound turn-by-turn on metal cylinders with radii of 3.5 mm, 2.5 mm and 1.5 mm, respectively, in such a way that the section with inscribed FBGs was placed in the middle of the winding. The values of the radii of curvature were calculated according to the method described in Section 2, where the radius of curvature is  $R = 1/|\kappa|$ . The corresponding results are shown in Table 3, where for the reference  $R_{\text{ref}}$  values, the distance from the cylinder surface to the neutral axis of the MCF is taken into account. The record small curvature radius of 2.58 mm is measured with an error less than 1%. To the best of our knowledge, the smallest measured bending radius, reported previously, was 14.3 mm with an error of 1.6% [16]. Also, we should mention that we did not observe any spectra distortions when curvature radius is comparable with FBG length (see Fig. 9).

**Table 3. Results of small radii of curvature measurement**

$R_{\text{ref}}$ , mm	$R_{\text{meas}}$ , mm	Rel. error, %
3.58	3.54	0.98
2.58	2.60	0.94
1.58	(fiber breakage)	(fiber breakage)

The fiber broke in the area of the FBG array when winding it on a cylinder with a radius of 1.5 mm, which corresponds to a deformation of 2.5% in the inscription area, and of 4% on the surface of the glass fiber cladding. It is important to note that the magnitude of the strain on the cladding surface approximately corresponds to the maximum tensile strength of glass fibers [27].

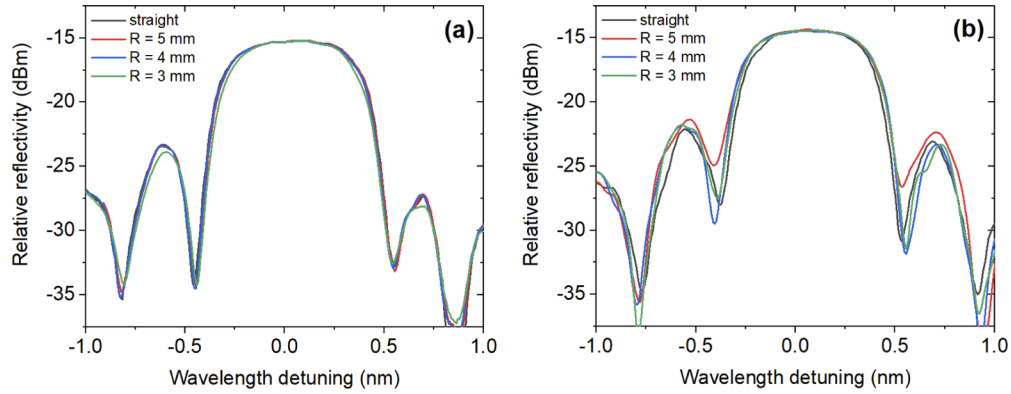


**Fig. 9.** FBG spectra at different radii of curvature for the central core (a) and for one of the side cores (b) subjected to a maximum bending strain.

In a distributed shape sensor, the limit of the minimum measurable radii is defined by several factors: 1) the spectral range of the interrogator and its wavelength resolution/repeatability reproducibility, 2) the number of FBGs in one core, their spectral width and, accordingly, the spectral interval between adjacent FBGs, 3) the length of the FBG and the distance between adjacent nodes. In our case, in each of the cores, the resonance wavelengths of the FBGs with a spectral width of 0.6–0.8 nm were distributed uniformly in the spectral range of the interrogator (1500–1600 nm). This ensured freedom of movement of the resonance peaks in the spectral region of about  $\pm 8$  nm. Knowing the sensitivity of the FBGs to bending ( $\Delta\lambda_{\max}/(1/R)$  is from 0.046 to 0.049 nm/m<sup>-1</sup>), we can estimate the minimum radius  $R_{\min} \sim 5.75$ –6.16 mm, when the FBGs adjacent in the spectral range do not overlap with each other. This may be the case if the curvature direction is changing by 180° from one node to another. With a constant number of FBGs and fixed spectral range of the interrogator,  $R_{\min}$  can be reduced by a closer arrangement of the cores, which however will lead to a decrease in the sensitivity of the FBG to bending.

To reveal the maximum measurable radii of the proposed sensor we carried out the experiment on the curve reconstruction with radius of curvature in the range from 100 to 500 mm. The results are presented in Table 4 and Fig. 10. The averaged relative error of radius measurement is less than 8% up to  $R = 350$  mm, while the absolute shape reconstruction error  $\delta_{\text{abs}}$  did not exceed 1 mm. The relative error significantly increases at the curvature radius of 500 mm and exceeds 14% with a high value of standard deviation. To understand the reason, we analyzed the influence of polarization effects on the error of curvature measurements. In case of large radii, the spectral shift of FBG decreases in comparison with small radii of curvature and for this reason this shift might be comparable with wavelength fluctuation  $\Delta\lambda_p$  associated with intrinsic birefringence of FBG. In our case the measured value  $\Delta\lambda_p$  is  $\approx 40$  pm that is comparable to point-by-point writing method [28]. Assuming this value, we can estimate the birefringence caused error of curvature radius measurements. For the ideal case  $R = k/\Delta\lambda$ , and  $R' = k/(\Delta\lambda \pm \lambda_p/2)$  when the polarization induced deviation is introduced. Thus, the relative error

$$\frac{\delta R}{R} = \frac{|R' - R|}{R} = \left| \frac{k}{k \pm R\Delta\lambda_p/2} - 1 \right|. \quad (8)$$

The relative error  $\delta R/R$  for  $\Delta\lambda_p = 40$  pm and  $k = 0.047$  nm/m<sup>-1</sup> as a function of curvature radius is plotted in Fig. 10. Also for comparison the results of error estimation based on  $\Delta\lambda_p = 20$  pm is presented. As one can see, the error of large curvature radii measurements obtained in the experiment can be associated with errors caused by  $\Delta\lambda_p = 20$ –40 pm. For this reason, to reduce this error for large curvature radii the value of  $\Delta\lambda_p$  should be minimized.

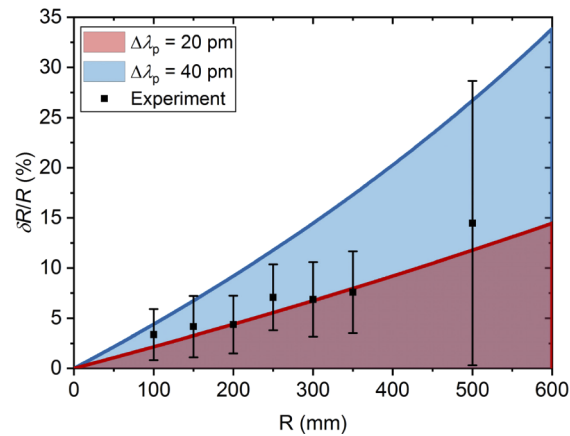


**Fig. 10.** The relative measurement error vs radius of curvature (dots), the estimation of influence of  $\Delta\lambda_p$  on relative error according to Eq. (8) (filled area).

**Table 4. Results of large radii of curvature measurement**

$R_{\text{ref}}$ , mm	100	150	200	250	300	350	500
$R_{\text{meas}}$ , mm	$97.9 \pm 3.7$	$145.3 \pm 6.2$	$198.7 \pm 10.5$	$239 \pm 16.3$	$289.1 \pm 21$	$347.9 \pm 30.6$	$551.9 \pm 96$
Rel. error, %	$3.4 \pm 2.5$	$4.2 \pm 3.1$	$4.4 \pm 2.9$	$7.1 \pm 3.3$	$6.9 \pm 3.7$	$7.6 \pm 4.1$	$14.5 \pm 14.2$

The thermal stability of FBG structures inscribed in a 7-core fiber with a polyimide protective coating was investigated for temperatures up to 330 °C. A sample of array consisting of 5 FBGs with reflection coefficient in range of 60–80%, and resonance wavelengths around 1550 nm, was inscribed in the central core of the MCF. The fabricated sample was annealed at 330 °C for 20 hours before the control experiment, in order to minimize the influence on the FBG reflection of temperature-dependent refractive index changes of the glass. It is known that femtosecond-pulse induced refractive index changes can be associated with the formation of different types of defects, including nonbridging oxygen hole center, SiE' centers, non-isotropic stress, and glass components migration [29]. This annealing temperature was chosen because the relaxation of color centers and internal stress occurs at around 300 °C and higher [30]. At the same time, the

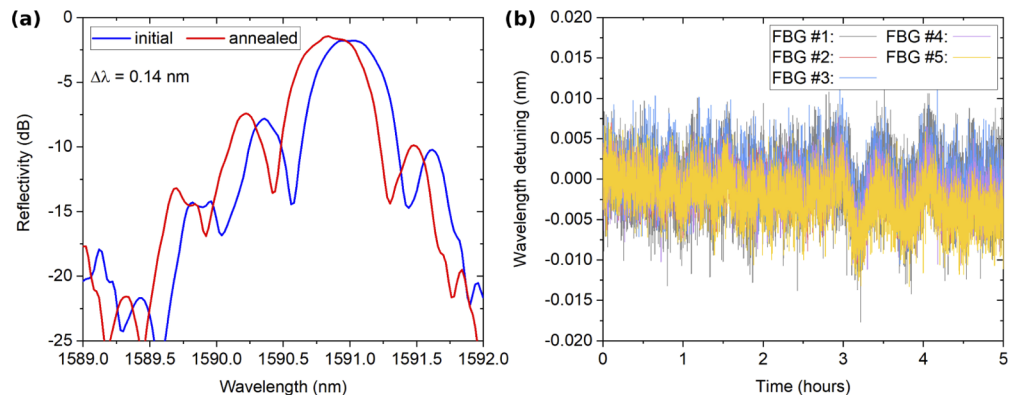


**Fig. 11.** (a) FBG spectra before and after the annealing process at room temperature, (b) resonant wavelength detuning depending on time at 330 °C.

polyimide protective coating is not significantly damaged at this temperature, and the optical fiber retains most of its mechanical strength [31]. In Fig. 11(a) the part of spectrum for one of the FBGs measured before and after annealing is shown. After the annealing process the resonance peak shifts to the short-wavelength region by 0.14 nm. This change is associated with a decrease in the effective refractive index in the area of the FBG. After sample annealing, we carried out a 5-hour control experiment at 330 °C in order to study the stability of the spectral characteristics of the FBG array. During this experiment, spectra were collected at intervals of 4 seconds. The time dependences of the resonant wavelengths are presented in Fig. 11(b) and revealed insignificant wavelength change less than 5 pm.

## 6. Conclusions

A temperature resistant fiber 3D shape sensor based on a polyimide coated custom-made 7-core optical fiber was fabricated and tested. We wrote an FBG array consisting of 6 nodes, with 4 FBGs in each node, located in the central core and in three side cores, by using a modified plane-by-plane femtosecond laser direct inscription method. The fabricated sensor was calibrated at different bending curvatures, in order to obtain individual bending sensitivities for each FBG in the array, which allowed for a precise shape sensing, with a positional error of less than 0.2 mm in the case of planar shapes. As a test of 3D shape configuration, spiral shapes were chosen: in this case the mean maximum deviation was of about 1.57 mm, which is mainly due to the uncompensated twist of the fiber and polarization sensitivity of FBG in the array. The possibility of measuring extremely small radii of curvature was demonstrated with an additionally fabricated single-node bending sensor, which showed the record ~1% error when measuring the radius of curvature of 2.6 mm. The measurements of lower radius of curvature is limited by fiber mechanical strength. The experiments of curves reconstruction at large radius of curvature in the range from 100 to 500 mm revealed the increase of reconstruction error due to the fact that wavelength shift in the side cores is comparable with polarization detuning of FBG wavelength that is a limiting factors in case of large radii of curvature. The thermal test of inscribed FBGs showed that after annealing the wavelength shift is insignificant (less than 5 pm) over 5 hours.

Considering the high mechanical durability and the small thickness of the polyimide coating, when compared with the commonly used acrylate polymer, in combination with the demonstrated temperature stability, the presented fiber shape sensor may be an attractive tool for robotics, structural monitoring in harsh environments, manufacturing of “smart” composites, as well as for minimally invasive surgery and biomedical devices.

## Funding

Ministry of Education and Science of the Russian Federation (14.Y26.31.0017).

## Disclosures

The authors declare no conflicts of interest.

## References

1. F. Khan, A. Denasi, D. Barrera, J. Madrigal, S. Sales, and S. Misra, “Multi-Core Optical Fibers With Bragg Gratings as Shape Sensor for Flexible Medical Instruments,” *IEEE Sens. J.* **19**(14), 5878–5884 (2019).
2. P. S. Westbrook, T. Kremp, K. S. Feder, W. Ko, E. M. Monberg, H. Wu, D. A. Simoff, T. F. Taunay, and R. M. Ortiz, “Continuous Multicore Optical Fiber Grating Arrays for Distributed Sensing Applications,” *J. Lightwave Technol.* **35**(6), 1248–1252 (2017).
3. L. A. Fernandes, J. R. Grenier, J. S. Aitchison, and P. R. Herman, “Fiber optic stress-independent helical torsion sensor,” *Opt. Lett.* **40**(4), 657–660 (2015).
4. S. Klute, R. Duncan, R. Fielder, G. Butler, J. Mabe, A. Sang, R. Seeley, and M. Raum, “Fiber-Optic Shape Sensing and Distributed Strain Measurements on a Morphing Chevron,” in *44th AIAA Aerospace Sciences Meeting and Exhibit*, Aerospace Sciences Meetings (American Institute of Aeronautics and Astronautics, 2006).



5. B. J. Soller, D. K. Gifford, M. S. Wolfe, and M. E. Froggatt, "High resolution optical frequency domain reflectometry for characterization of components and assemblies," *Opt. Express* **13**(2), 666–674 (2005).
6. K. K. C. Lee, A. Mariampillai, M. Haque, B. A. Standish, V. X. D. Yang, and P. R. Herman, "Temperature-compensated fiber-optic 3D shape sensor based on femtosecond laser direct-written Bragg grating waveguides," *Opt. Express* **21**(20), 24076–24086 (2013).
7. M. Weisbrich and K. Holschemacher, "Comparison between different fiber coatings and adhesives on steel surfaces for distributed optical strain measurements based on Rayleigh backscattering," *J. Sens. Sens. Syst.* **7**(2), 601–608 (2018).
8. K. Satori, K. Fukuchi, Y. Kurosawa, A. Hongo, and N. Takeda, "Polyimide-coated small-diameter optical fiber sensors for embedding in composite laminate structures," in *Smart Structures and Materials 2001: Sensory Phenomena and Measurement Instrumentation for Smart Structures and Materials* (International Society for Optics and Photonics, 2001), 4328, pp. 285–294.
9. V. V. Shishkin, V. S. Terentyev, D. S. Kharenko, A. V. Dostovalov, A. A. Wolf, V. A. Simonov, M. Y. Fedotov, A. M. Shienok, I. S. Shelemba, and S. A. Babin, "Experimental Method of Temperature and Strain Discrimination in Polymer Composite Material by Embedded Fiber-Optic Sensors Based on Femtosecond-Inscribed FBGs," *J. Sens.* **2016**, 1–6 (2016).
10. S.-Y. Yang and M. Ji, "Chapter 3 - Polyimide Matrices for Carbon Fiber Composites," in *Advanced Polyimide Materials*, S.-Y. Yang, ed. (Elsevier, 2018), pp. 93–136.
11. A. A. Stolov, D. A. Simoff, and J. Li, "Thermal Stability of Specialty Optical Fibers," *J. Lightwave Technol.* **26**(20), 3443–3451 (2008).
12. J. Canning, "Fibre gratings and devices for sensors and lasers," *Laser Photonics Rev.* **2**(4), 275–289 (2008).
13. R. R. Gattass and E. Mazur, "Femtosecond laser micromachining in transparent materials," *Nat. Photonics* **2**(4), 219–225 (2008).
14. A. V. Dostovalov, A. A. Wolf, A. V. Parygin, V. E. Zyubin, and S. A. Babin, "Femtosecond point-by-point inscription of Bragg gratings by drawing a coated fiber through ferrule," *Opt. Express* **24**(15), 16232–16237 (2016).
15. A. Martinez, I. Y. Khrushchev, and I. Bennion, "Thermal properties of fibre Bragg gratings inscribed point-by-point by infrared femtosecond laser," *Electron. Lett.* **41**(4), 176–178 (2005).
16. J. P. Moore and M. D. Rogge, "Shape sensing using multi-core fiber optic cable and parametric curve solutions," *Opt. Express* **20**(3), 2967–2973 (2012).
17. C. D. Butter and G. B. Hocker, "Fiber optics strain gauge," *Appl. Opt.* **17**(18), 2867–2869 (1978).
18. A. T. Fomenko and A. S. Mishchenko, *A Short Course in Differential Geometry and Topology* (Cambridge Scientific Publishers, 2009).
19. V. Budinski and D. Donlagic, "Fiber-Optic Sensors for Measurements of Torsion, Twist and Rotation: A Review," *Sensors* **17**(3), 443 (2017).
20. I. Gasulla, D. Barrera, J. Hervás, and S. Sales, "Spatial Division Multiplexed Microwave Signal processing by selective grating inscription in homogeneous multicore fibers," *Sci. Rep.* **7**(1), 41727 (2017).
21. A. Donko, M. Beresna, Y. Jung, J. Hayes, D. J. Richardson, and G. Brambilla, "Point-by-point femtosecond laser micro-processing of independent core-specific fiber Bragg gratings in a multi-core fiber," *Opt. Express* **26**(2), 2039–2044 (2018).
22. P. Lu, S. J. Mihailov, H. Ding, D. Grobnc, R. B. Walker, D. Coulas, C. Hnatovsky, and A. Y. Naumov, "Plane-by-Plane Inscription of Grating Structures in Optical Fibers," *J. Lightwave Technol.* **36**(4), 926–931 (2018).
23. A. Wolf, A. Dostovalov, K. Bronnikov, and S. Babin, "Arrays of fiber Bragg gratings selectively inscribed in different cores of 7-core spun optical fiber by IR femtosecond laser pulses," *Opt. Express* **27**(10), 13978–13990 (2019).
24. O. N. Egorova, M. E. Belkin, D. A. Klushnik, S. G. Zhuravlev, M. S. Astapovich, and S. L. Semojnov, "Microwave signal delay line based on multicore optical fiber," *Phys. Wave Phen.* **25**(4), 289–292 (2017).
25. A. Morana, S. Girard, E. Marin, C. Marcandella, P. Paillet, J. Périsse, J.-R. Macé, A. Boukenter, M. Cannas, and Y. Ouerdane, "Radiation tolerant fiber Bragg gratings for high temperature monitoring at MGy dose levels," *Opt. Lett.* **39**(18), 5313–5316 (2014).
26. J. Albert, L.-Y. Shao, and C. Caucheteur, "Tilted fiber Bragg grating sensors," *Laser Photonics Rev.* **7**(1), 83–108 (2013).
27. M. Bernier, F. Trépanier, J. Carrier, and R. Vallée, "High mechanical strength fiber Bragg gratings made with infrared femtosecond pulses and a phase mask," *Opt. Lett.* **39**(12), 3646–3649 (2014).
28. Y. Lai, K. Zhou, K. Sugden, and I. Bennion, "Point-by-point inscription of first-order fiber Bragg grating for C-band applications," *Opt. Express* **15**(26), 18318–18325 (2007).
29. K. Itoh, W. Watanabe, S. Nolte, and C. B. Schaffer, "Ultrafast Processes for Bulk Modification of Transparent Materials," *MRS Bull.* **31**(8), 620–625 (2006).
30. A. M. Streltsov and N. F. Borrelli, "Study of femtosecond-laser-written waveguides in glasses," *J. Opt. Soc. Am. B* **19**(10), 2496–2504 (2002).
31. L. Huang, R. S. Dyer, R. J. Lago, A. A. Stolov, and J. Li, "Mechanical properties of polyimide coated optical fibers at elevated temperatures," in *Optical Fibers and Sensors for Medical Diagnostics and Treatment Applications XVI* (International Society for Optics and Photonics, 2016), 9702, p. 97020Y.